

Nuclear deformation in the laboratory frame

C.N. Gilbreth,¹ Y. Alhassid,² and G.F. Bertsch^{1,3}

¹*Institute of Nuclear Theory, Box 351550, University of Washington, Seattle, WA 98195*

²*Center for Theoretical Physics, Sloane Physics Laboratory, Yale University, New Haven, CT 06520*

³*Department of Physics, Box 351560, University of Washington, Seattle, WA 98195*

(Dated: October 11, 2017)

We develop a formalism for calculating the distribution of the axial quadrupole operator in the laboratory frame within the rotationally invariant framework of the configuration-interaction shell model. The calculation is carried out using a finite-temperature auxiliary-field quantum Monte Carlo method. We apply this formalism to isotope chains of even-mass samarium and neodymium nuclei, and show that the quadrupole distribution provides a model-independent signature of nuclear deformation. Two technical advances are described that greatly facilitate the calculations. The first is to exploit the rotational invariance of the underlying Hamiltonian to reduce the statistical fluctuations in the Monte Carlo calculations. The second is to determine quadrupole invariants from the distribution of the axial quadrupole operator. This allows us to extract effective values of the intrinsic quadrupole shape parameters without invoking an intrinsic frame or a mean-field approximation.

PACS numbers: 21.60.Cs, 21.60.Ka, 21.10.Ma, 02.70.Ss

I. INTRODUCTION

Although the Hamiltonian of an atomic nucleus is rotationally invariant, open-shell nuclei often exhibit features that are qualitatively well-described by simple models in which the nucleus is deformed rather than spherical. In particular, deformed nuclei show rotational bands of energy levels consistent with the model of an axially symmetric rigid rotor [1].

Deformation is typically introduced through a mean-field approximation that breaks the rotational symmetry of the underlying Hamiltonian. For instance, the axial quadrupole operator $\hat{Q}_{2\mu}$, which measures quadrupole deformations, acquires a nonzero expectation in the solution to the Hartree-Fock (HF) or Hartree-Fock-Bogoliubov (HFB) equations for deformed nuclei. However, the exact expectation values of $\hat{Q}_{2\mu}$ are always zero for a nucleus described by a rotationally-invariant Hamiltonian. Because atomic nuclei do exhibit signatures of deformation, yet they are described by a rotationally invariant Hamiltonian, it is of interest to be able to extract information about nuclear deformation within a framework that preserves rotational invariance and without invoking a mean-field approximation.

In Ref. [2] we introduced a method to extract signatures of nuclear deformation from auxiliary-field quantum Monte Carlo (AFMC) simulations in the framework of the spherical configuration-interaction (CI) shell model. The method works by examining the finite-temperature distributions of the axial quadrupole operator \hat{Q}_{20} in the laboratory frame. Here we expand upon the details of the method, describing the calculation of this distribution and how to overcome an equilibration and decorrelation problem for deformed nuclei. Our current methodology was demonstrated in Ref. [2] for the spherical nucleus ^{148}Sm and the deformed nucleus ^{154}Sm . Here we extend the applications to isotope chains of even-

mass samarium and neodymium nuclei which exhibit a crossover from spherical to deformed shapes.

We use quadrupole invariants [3, 4], defined in the framework of the CI shell model, to extract information on the effective intrinsic quadrupole deformation. This aspect is independent of the method used to determine the invariants. For nuclei lighter than the ones considered here, the CI shell model has also been successfully employed. See Refs. [5, 6] for recent examples and for other references cited therein. We note the AFMC has been previously applied to calculate intrinsic shape distributions [7] but there an ad hoc prescription was used for extracting shape information.

The outline of this paper is as follows. In Sec. II we review briefly the finite-temperature AFMC method. In Sec. III, we discuss the formalism for projecting onto the axial quadrupole operator in order to calculate its lab-frame finite-temperature distribution using AFMC. Furthermore, we present an angle-averaging method to help equilibrating this distribution and reduce the decorrelation length in its sampling. In Sec. IV we apply the method to the deformed nucleus ^{162}Dy and to two isotope chains of lanthanide nuclei in which we observe a crossover from spherical to deformed behavior. We compare our AFMC results with the finite-temperature HFB mean-field approximation [8, 9]. In Sec. V, we discuss low-order quadrupole invariants and their relation to the moments of the axial quadrupole operator in the laboratory frame. These invariants are used to extract effective intrinsic quadrupole deformation parameters in the rotationally invariant framework of the CI shell model, without the use of a mean-field approximation. We conclude with a summary and outlook in Sec. VI. Some of the technical details are discussed in the Appendices. Finally, the data files containing the AFMC and HFB results presented in this work are included in the Supplementary Material depository of this article.

II. AUXILIARY-FIELD MONTE CARLO METHOD

We briefly review the AFMC method, also known as shell model Monte Carlo (SMMC) in the context of the nuclear shell model [10–12]. For a nucleus at a finite temperature T , we consider its imaginary-time propagator $e^{-\beta\hat{H}}$, which describes the Gibbs ensemble at inverse temperature $\beta = 1/T$ for a Hamiltonian \hat{H} .¹ The AFMC method is based on the Hubbard-Stratonovich transformation [13], in which the Gibbs propagator $e^{-\beta\hat{H}}$ is decomposed into a superposition of imaginary-time evolution operators \hat{U}_σ of non-interacting nucleons

$$e^{-\beta\hat{H}} = \int \mathcal{D}[\sigma] G_\sigma \hat{U}_\sigma, \quad (1)$$

where G_σ is a Gaussian weight and σ are auxiliary fields that depend on imaginary time τ ($0 \leq \tau \leq \beta$).

The thermal expectation value of an observable \hat{O} is then given by

$$\langle \hat{O} \rangle = \frac{\text{Tr}(\hat{O}e^{-\beta\hat{H}})}{\text{Tr}(e^{-\beta\hat{H}})} = \frac{\int \mathcal{D}[\sigma] G_\sigma \langle \hat{O} \rangle_\sigma \text{Tr} \hat{U}_\sigma}{\int \mathcal{D}[\sigma] G_\sigma \text{Tr} \hat{U}_\sigma}, \quad (2)$$

where $\langle \hat{O} \rangle_\sigma \equiv \text{Tr}(\hat{O}\hat{U}_\sigma)/\text{Tr} \hat{U}_\sigma$ is the expectation value of \hat{O} for non-interacting particles in external auxiliary fields $\sigma(\tau)$.

The grand-canonical traces can be evaluated by reducing them to quantities in the single-particle space. For example, the grand-canonical partition function for a given configuration of the fields σ is

$$\text{Tr} \hat{U}_\sigma = \det(\mathbf{1} + \mathbf{U}_\sigma), \quad (3)$$

where \mathbf{U}_σ is the matrix representation of \hat{U}_σ in the single-particle space.

The Monte Carlo sampling of the fields σ is carried out using the positive-definite weight function

$$W_\sigma \equiv G_\sigma |\text{Tr} \hat{U}_\sigma|. \quad (4)$$

We define the W -weighted average of a quantity X_σ that depends on the auxiliary-field configuration σ by

$$\langle X_\sigma \rangle_W \equiv \frac{\int D[\sigma] W_\sigma X_\sigma \Phi_\sigma}{\int D[\sigma] W_\sigma \Phi_\sigma}, \quad (5)$$

where

$$\Phi_\sigma \equiv \text{Tr} U_\sigma / |\text{Tr} U_\sigma| \quad (6)$$

is the Monte Carlo sign function. With this definition, the thermal expectation of an observable \hat{O} can be written as

$$\langle \hat{O} \rangle = \left\langle \frac{\text{Tr}(\hat{O}\hat{U}_\sigma)}{\text{Tr} \hat{U}_\sigma} \right\rangle_W. \quad (7)$$

¹ We will use the circumflex to denote operators in the many-particle Fock space.

We can also carry out projections on conserved one-body observables, such as particle number [14, 15] and total angular momentum [16]. In particular, the canonical partition $\text{Tr}_\mathcal{A} \hat{U}_\sigma$ for fixed particle number \mathcal{A} can be calculated by the discrete Fourier transform

$$\text{Tr}_\mathcal{A} U_\sigma = \frac{e^{-\beta\mu\mathcal{A}}}{N_s} \sum_{m=1}^{N_s} e^{-i\chi_m\mathcal{A}} \det(\mathbf{1} + e^{i\chi_m} e^{\beta\mu} \mathbf{U}_\sigma), \quad (8)$$

where N_s is the number of single-particle orbitals, $\chi_m = 2\pi m/N_s$ ($m = 1, \dots, N_s$) are quadrature points and μ is a chemical potential introduced to stabilize the numerical evaluation of the Fourier sum.

In practice, we always work in the canonical ensemble and calculate the expectation values of observables at fixed proton and neutron numbers, i.e., $\mathcal{A} = (Z, N)$. We then replace the traces in Eqs. (2,4-7) by canonical traces, i.e., $\text{Tr} \rightarrow \text{Tr}_\mathcal{A}$.

III. PROJECTION ON THE AXIAL QUADRUPOLE OPERATOR \hat{Q}_{20} IN THE LABORATORY FRAME

A. Projection formalism

The probability distribution of the axial quadrupole operator $\hat{Q}_{20} = \sum_i (2z_i^2 - x_i^2 - y_i^2)$ at inverse temperature β is defined by

$$P_\beta(q) = \text{Tr}[\delta(\hat{Q}_{20} - q)e^{-\beta\hat{H}}] / \text{Tr}e^{-\beta\hat{H}}, \quad (9)$$

where $q \equiv q_{20}$ and $\delta(\hat{Q}_{20} - q)$ projects onto the eigenspace corresponding to eigenvalue q of \hat{Q} . The Monte Carlo expectation of $P_\beta(q)$ is then

$$P_\beta(q) = \left\langle \frac{\text{Tr}[\delta(\hat{Q}_{20} - q)\hat{U}_\sigma]}{\text{Tr} \hat{U}_\sigma} \right\rangle_W. \quad (10)$$

Expanding the distribution (9) in terms of many the many-particle eigenstates $|q_n\rangle$ and $|e_m\rangle$ of \hat{Q}_{20} and \hat{H} , respectively, we find

$$P_\beta(q) = \sum_n \delta(q - q_n) \sum_m \langle q_n | e_m \rangle^2 e^{-\beta e_m}. \quad (11)$$

$P_\beta(q)$ represents the probability of measuring eigenvalue q of \hat{Q}_{20} in the finite-temperature Gibbs ensemble. Since the quadrupole operator \hat{Q}_{20} does not commute with the Hamiltonian, there does not exist a basis of simultaneous eigenstates of \hat{Q}_{20} and \hat{H} , unlike for projections onto conserved one-body observables. Nevertheless, the quadrupole distribution in a thermal ensemble is well-defined and is given by Eq. (11).

The expression (11) is impractical for realistic calculations, since the sums over n, m range over bases of many-particle states. However, the distribution $P_\beta(q)$ can be

calculated using the Fourier representation of the δ function

$$\delta(\hat{Q}_{20} - q) = \frac{1}{2\pi} \int_{-\infty}^{\infty} d\varphi e^{-i\varphi q} e^{i\varphi \hat{Q}_{20}}. \quad (12)$$

Up to now, we have treated q as a continuous variable. Since the AFMC works in a finite model space, \hat{Q}_{20} has a discrete and finite spectrum. However, for heavy nuclei, the many-body eigenvalues of \hat{Q}_{20} are sufficiently closely spaced to allow q to be approximated as continuous.

For a given \hat{U}_σ , the projection is carried out using a discretized version of the Fourier decomposition in Eq. (12). We take an interval $[-q_{\max}, q_{\max}]$ and divide it into $2M + 1$ equal intervals of length $\Delta q = 2q_{\max}/(2M + 1)$. We define $q_m = m\Delta q$, where $m = -M, \dots, M$, and approximate the quadrupole-projected trace in (10) by

$$\text{Tr} [\delta(\hat{Q}_{20} - q_m) \hat{U}_\sigma] \approx \frac{1}{2q_{\max}} \sum_{k=-M}^M e^{-i\varphi_k q_m} \text{Tr}(e^{i\varphi_k \hat{Q}_{20}} \hat{U}_\sigma), \quad (13)$$

where $\varphi_k = \pi k/q_{\max}$ ($k = -M, \dots, M$).

Since \hat{Q}_{20} is a one-body operator and \hat{U}_σ is a one-body propagator, the grand-canonical many-particle trace on the r.h.s. of Eq. (13) reduces to a determinant in the single-particle space

$$\text{Tr} \left(e^{i\varphi_k \hat{Q}_{20}} \hat{U}_\sigma \right) = \det \left(1 + e^{i\varphi_k \mathbf{Q}_{20}} \mathbf{U}_\sigma \right), \quad (14)$$

where \mathbf{Q}_{20} and \mathbf{U}_σ are the matrices representing, respectively, \hat{Q}_{20} and \hat{U}_σ , in the single-particle space. Projections are also carried on the proton and proton number operators to fix the Z and N of the ensemble.

B. Angle averaging and thermalization

The thermalization and decorrelation of moments of \hat{Q}_{20} are very slow for deformed nuclei when using the pure Metropolis sampling. This can be overcome by augmenting the Metropolis-generated configurations by rotating them through a properly chosen set of N_Ω rotation angles Ω_i . In practice, it is easier to rotate the matrix \mathbf{U}_σ . We make the replacement

$$\langle e^{i\varphi \hat{Q}_{20}} \rangle_\sigma \rightarrow \frac{1}{N_\Omega} \sum_{j=1}^{N_\Omega} \langle e^{i\varphi \hat{Q}_{20}} \rangle_{\sigma, \Omega_j}, \quad (15)$$

where

$$\langle \hat{X} \rangle_{\sigma, \Omega} = \frac{\text{Tr} \left[\hat{X} \left(\hat{R}(\Omega) \hat{U}_\sigma \hat{R}^\dagger(\Omega) \right) \right]}{\text{Tr} \left[\hat{R}(\Omega) \hat{U}_\sigma \hat{R}^\dagger(\Omega) \right]}, \quad (16)$$

and where $\hat{R}(\Omega)$ is the rotation operator for angle Ω .

In the following we discuss methods for choosing these angles. The main observation is that quadrupole invariants such as $Q \cdot Q$ thermalize faster than moments of

\hat{Q}_{20} . For a rotationally invariant system, the low moments of \hat{Q}_{20} are proportional to the expectation values of quadrupole invariants (see Eqs. (31-33) below). In AFMC, these relations hold only on average, i.e., only after averaging over all auxiliary-field configurations. If we can choose a set of rotation angles Ω_i such the angle-averaged moment of \hat{Q}_{20} is equal to the corresponding invariant (as operators), then the relations (31-33) will hold sample-by-sample. We will show that this leads to a faster thermalization and decorrelation of the corresponding moment of \hat{Q}_{20} .

1. Six-angle averaging

Here, we find a set of six angles for which the angle-averaged \hat{Q}_{20}^2 is proportional to the second-order invariant $\hat{Q} \cdot \hat{Q}$.

The second moment of \hat{Q}_{20} is related to the second-order quadrupole invariant $\langle \hat{Q} \cdot \hat{Q} \rangle$ by $\langle \hat{Q}_{20}^2 \rangle = \langle \hat{Q} \cdot \hat{Q} \rangle/5$. We would like to find a set of angles Ω_i such that

$$\sum_i \hat{R}(\Omega_i) \hat{Q}_{20}^2 \hat{R}^\dagger(\Omega_i) \propto \hat{Q} \cdot \hat{Q}. \quad (17)$$

To determine an appropriate set of angles, we rotate each factor of \hat{Q}_{20} to obtain

$$\begin{aligned} \sum_i \hat{R}(\Omega_i) \hat{Q}_{20}^2 \hat{R}^\dagger(\Omega_i) \\ = \sum_{\mu, \mu'} \left(\sum_i D_{\mu 0}^{(2)}(\Omega_i) D_{\mu' 0}^{(2)}(\Omega_i) \right) \hat{Q}_{2\mu} \hat{Q}_{2\mu'}, \end{aligned} \quad (18)$$

where $D^{(2)}(\Omega)$ is the corresponding Wigner matrix for a rotation angle Ω . The required condition is thus

$$\sum_i D_{\mu 0}^{(2)}(\Omega_i) D_{\mu' 0}^{(2)}(\Omega_i) \propto (-)^\mu \delta_{\mu, -\mu'}. \quad (19)$$

To find the appropriate angles for which (19) holds, note that $D_{\mu 0}^{(2)}(\varphi, \theta, \psi) = \sqrt{\frac{4\pi}{5}} Y_{2\mu}(\theta, \varphi) \propto P_2^0(\cos \theta) e^{i\mu\varphi}$. The Kronecker delta $\delta_{\mu, -\mu'}$ can be obtained by summing over five angles $\varphi_k = \frac{2\pi k}{5}$, $k = 0, 1, \dots, 4$ using the identity $\sum_{k=0}^4 e^{2\pi i k(\mu + \mu')/5} = 5\delta_{\mu, -\mu'}$. Then

$$\sum_{k=0}^4 D_{\mu 0}^{(2)}(\theta, \varphi_k) D_{\mu' 0}^{(2)}(\theta, \varphi_k) = 5\delta_{\mu, -\mu'} P_2^\mu(\cos \theta) P_2^{-\mu}(\cos \theta) \quad (20)$$

for any θ . Choosing a particular angle θ_1 by $\cos^2 \theta_1 = 1/5$, we have

$$P_2^\mu(\cos \theta_1) P_2^{-\mu}(\cos \theta_1) = \begin{cases} 1/5, & \mu = 0 \\ -6/5, & \mu = \pm 1 \\ 6/5, & \mu = \pm 2 \end{cases}. \quad (21)$$

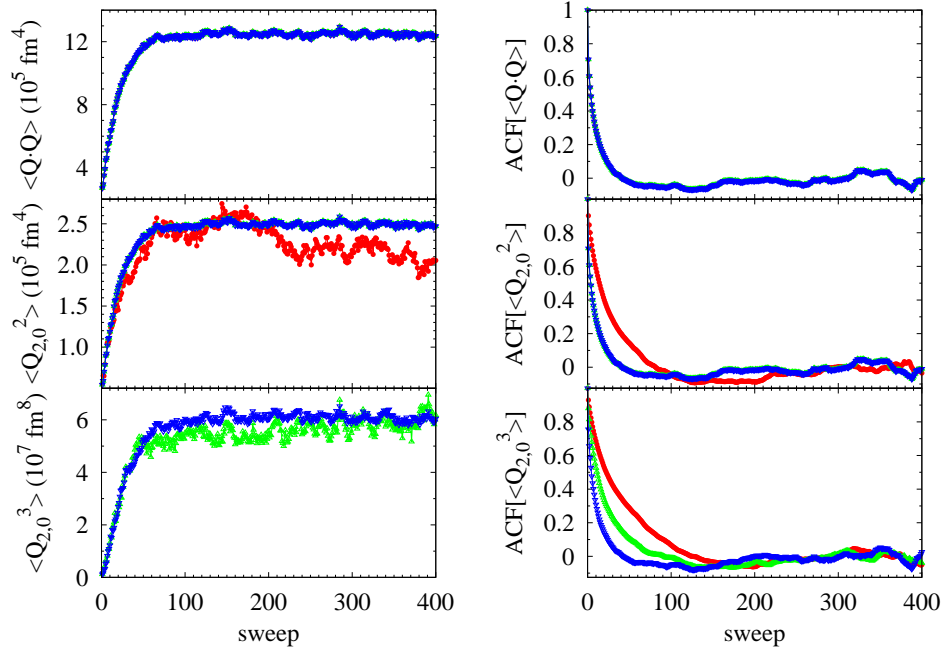


FIG. 1. Equilibration (left column) and autocorrelation function (right column) of the invariant $\langle \hat{Q} \cdot \hat{Q} \rangle$ (top panels), and of the quadrupole moments $\langle \hat{Q}_{20}^2 \rangle$ and $\langle \hat{Q}_{20}^3 \rangle$, for several levels of angle-averaging: no averaging (red circles), six angles (green triangles), and 21 angles (blue inverted triangles). The horizontal axis shows the number of Monte Carlo sweeps (each sweep is one update of all auxiliary fields). In the top panels, the points overlap since $\langle \hat{Q} \cdot \hat{Q} \rangle$ is rotationally invariant sample-by-sample. In the bottom right panel, the no-averaging results have $\langle \hat{Q}_{20}^3 \rangle \sim 10^{10}$ and are above the range of the y-axis. Rotating by a sufficient number of angles to restore rotational invariance for \hat{Q}_{20}^2 and \hat{Q}_{20}^3 makes their Monte Carlo sampling behavior become very similar to that of $\langle \hat{Q} \cdot \hat{Q} \rangle$.

Adding the angle $\theta = 0, \varphi = 0$ at which $D_{\mu 0}^{(2)}(0, 0) = \delta_{\mu, 0}$, we obtain

$$\sum_{i=0}^5 D_{\mu 0}^{(2)}(\Omega_i) D_{\mu' 0}^{(2)}(\Omega_i) = \frac{6}{5} (-)^{\mu} \delta_{\mu, -\mu'}, \quad (22)$$

where $\Omega_0 = (0, 0)$ and $\Omega_i = (\theta_1, \varphi_{i-1})$ for $i = 1, \dots, 5$.

In Appendix A, we discuss a general method to determine a set of angles such that the angle-averaged moments of \hat{Q}_{20} are proportional to the quadrupole invariants of the same order up to the n -th order. For $n = 2$ and $n = 3$, this leads to a set of 10 and 21 angles, respectively. When averaging over the specific set of 21 angles, both the second and cubic moments of \hat{Q}_{20} are proportional to the second- and third-order quadrupole invariants, respectively, sample-by-sample.

We demonstrate the thermalization of moments of \hat{Q}_{20} for ^{154}Sm in the left column Fig. 1, in which we show the second moment $\langle \hat{Q}_{20}^2 \rangle$ (middle panel) and third moment $\langle \hat{Q}_{20}^3 \rangle$ (bottom panel) of \hat{Q}_{20} as a function of the sweep number in the Monte Carlo random walk. We compare the no angle averaging (red circles) with the 6-angle averaging (green triangles) and 21-angle averaging (blue inverted triangles). The top panel shows the direct calculation of the second-order quadrupole invariant $\langle \hat{Q} \cdot \hat{Q} \rangle$, which has no equilibration or decorrelation problem. One can see that $\langle \hat{Q}_{20}^2 \rangle$ for 6 and 21 angles, and $\langle \hat{Q}_{20}^3 \rangle$ for

21 angles, show smaller fluctuations and more rapid and obvious thermalization, very similar to the behavior of $\langle \hat{Q} \cdot \hat{Q} \rangle$.

On the right column of Fig. 1, we show the autocorrelation function (ACF) of the same observables and for similar levels of angle-averaging. The observable $\langle \hat{Q}_{20}^2 \rangle$ decorrelates faster in the six-angle averaging (as compared with the no-angle averaging results), while $\langle \hat{Q}_{20}^3 \rangle$ decorrelates fastest in the 21-angle averaging. We see that the improvement in thermalization is closely related to a shorter decorrelation length.

The thermalization of the second and third moments of \hat{Q}_{20} is important for the calculation of a distribution $P(q)$ that is independent of the choice of the initial seed. In Fig. 2 we show the quadrupole distribution for ^{154}Sm using different levels of angle-averaging, based on ~ 5000 Monte Carlo samples. In the AFMC calculations, it is necessary to discretize the imaginary time and we use a time slice of $\Delta\beta = 1/32 \text{ MeV}^{-1}$ here and in all the results presented in this work. The distribution obtained with no angle averaging (red line) is not thermalized, while the distribution with the six-angle average (blue line) is very close to the one obtained with 21-angle average (green line). In the applications presented in this work, we have used 21-angle averaging to make sure the calculated distributions $P(q)$ and moments of \hat{Q}_{20} are thermalized and have a short decorrelation length.

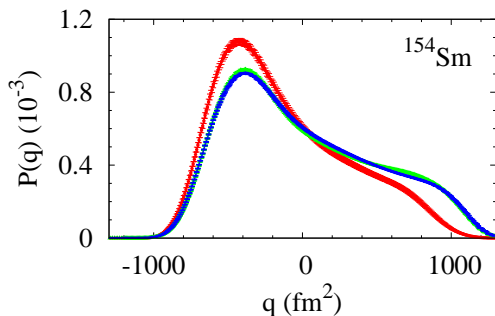


FIG. 2. Distribution $P(q)$ vs. q of ^{154}Sm at a low temperature for several levels of angle-averaging: no averaging (red symbols), six angles (green symbols), and 21 angles (blue symbols). The results from 6-angle and 21-angle averaging are hardly distinguishable.

IV. APPLICATION TO LANTHANIDES

Here we present results for rare-earth nuclei. We consider the deformed nucleus ^{162}Dy as well as the two isotope chains of even-even nuclei $^{144-152}\text{Nd}$ and $^{148-154}\text{Sm}$.

We compare some of the AFMC results with a mean-field approximation, the finite-temperature HFB approximation [8, 9], using the same model space and interaction as for our AFMC calculations. In the zero-temperature HFB, there is a phase transition from a spherical to a deformed shape as we increase the number of neutrons within each of these two isotope chains. In the finite-temperature HFB, an isotope which has a deformed HFB ground state undergoes a phase transition to a spherical shape at a certain critical temperature.

A. CI shell model space and interaction

The single-particle orbitals and energies are taken as eigenfunctions of a spherical Woods-Saxon potential plus a spin-orbit interaction. For protons we take the complete 50-82 shell plus the $1f_{7/2}$ orbital, and for neutrons the 82 – 126 shell plus the $0h_{11/2}$ and $1g_{9/2}$ orbitals. The interaction includes a monopole pairing interaction and multipole-multipole interactions with quadrupole, octupole and hexadecupole components. The interaction parameters are given in Refs. [17, 18].

B. Distributions $P_\beta(q)$

1. A deformed nucleus

In Fig. 3 we show the distributions $P_\beta(q)$ for ^{162}Dy at high temperature, near the HFB shape transition temperature, and at low temperature. Since our model space is restricted to valence shells, we scale q here and in other figures by a factor of 2 to account for effects of

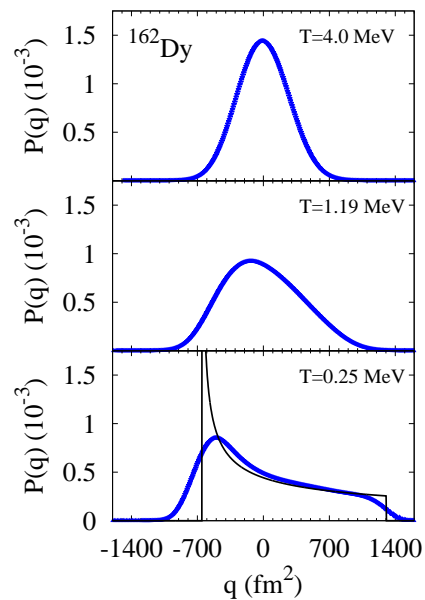


FIG. 3. Distributions $P(q)$ vs. q for ^{162}Dy at high temperature (top panel), near the HFB shape transition temperature (middle panel), and at low temperature (bottom panel). The low-temperature distribution is qualitatively similar to the rigid rotor ground-state distribution (solid line) with an intrinsic quadrupole moment q_0 taken to be the HFB value of $\langle \hat{Q}_{20} \rangle$.

the core. One expects the nucleus to resemble a rigid rotor at low temperatures. For a rigid rotor with an intrinsic quadrupole moment of $q_0 > 0$ (corresponding to a prolate shape), this distribution is [2]

$$P_{\text{g.s.}}(q) = \begin{cases} \left(\sqrt{3}q_0 \sqrt{1 + 2\frac{q}{q_0}} \right)^{-1} & \text{for } -\frac{q_0}{2} \leq q \leq q_0 \\ 0 & \text{otherwise} \end{cases} \quad (23)$$

We determine q_0 from the HFB value of $\langle \hat{Q}_{20} \rangle$ at $T = 0$. The rigid-rotor distribution shown in the bottom panel of Fig. 3 is qualitatively similar to the low-temperature distribution for ^{162}Dy .

The lab-frame moments of the distribution (23) are calculated in Appendix B.

2. A spherical nucleus

In Fig. 4 we illustrate the case of a spherical nucleus, ^{144}Nd . Here the quadrupole distribution is close to Gaussian at all temperatures, although it develops a slight skew at low temperatures.

We conclude that the distribution of the axial quadrupole in the laboratory frame is a model-independent signature of deformation.

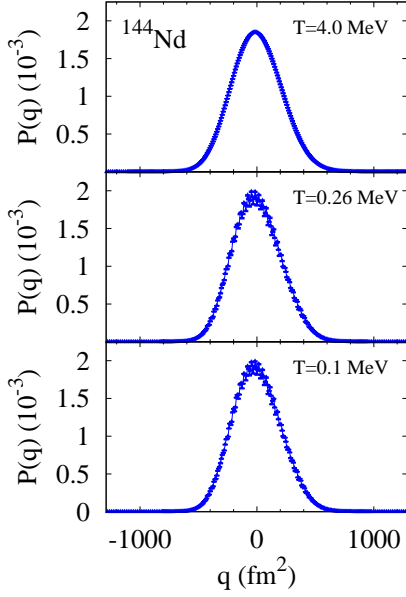


FIG. 4. Distributions $P(q)$ vs q for ^{144}Nd at high temperature (top panel), an intermediate temperature (middle panel), and at low temperature (bottom panel). The low-temperature distributions show a slight staggering effect and skew but are very close to Gaussian.

3. Crossover from spherical to deformed nuclei

In Figs. 5 and 6 we show the distributions $P_\beta(q)$ for isotope chains of samarium and neodymium nuclei at several temperatures. The low-temperature ($T = 0.1$ MeV) distributions display a crossover as a function of neutron number from spherical behavior in ^{148}Sm and ^{144}Nd to deformed behavior in ^{154}Sm and ^{152}Nd .

The nuclei that are deformed at low temperatures undergo a crossover to a spherical shape with increasing temperature. This transition from deformed to spherical shape is well-known in the HF and HFB mean-field theories where it is seen as a sharp phase transition [19–21]. Here we see it as a gradual change. The distributions $P_\beta(q)$ are still skewed above the mean-field transition temperature, indicating the persistence of deformation effects to high temperatures.

C. $\langle \hat{Q} \cdot \hat{Q} \rangle$ vs. temperature

We now compare in more detail the AFMC results to those of the finite-temperature HFB approximation. The HFB solution is described by temperature-dependent one-body density matrix ρ_β and pairing tensor κ_β . The second-order invariant $\langle \hat{Q} \cdot \hat{Q} \rangle$ is derived in HFB using

Wick's theorem, resulting in

$$\begin{aligned} \langle \hat{Q} \cdot \hat{Q} \rangle = q_0^2 + \sum_{\mu} (-)^{\mu} \text{tr} [\mathbf{Q}_{2\mu} (\mathbf{1} - \rho_\beta) \mathbf{Q}_{2-\mu} \rho_\beta] \\ + \sum_{\mu} (-)^{\mu} \text{tr} [\mathbf{Q}_{2\mu} \kappa_\beta \mathbf{Q}_{2-\mu}^T \kappa_\beta^*]. \end{aligned} \quad (24)$$

Here $q_0 \equiv \text{tr}(\mathbf{Q}_{20} \rho_\beta)$ is the intrinsic axial quadrupole moment.

In Figs. 7 and 8 we compare AFMC (blue solid circles) and HFB (solid lines) results for $\langle \hat{Q} \cdot \hat{Q} \rangle$ for the same isotope chains of samarium and neodymium nuclei. The HFB results show a sharp phase transition between spherical and deformed shapes as a function of temperature, while the AFMC shows a smooth crossover, as remarked earlier. For the deformed nuclei, $\langle \hat{Q} \cdot \hat{Q} \rangle$ is similar for the two methods at low temperature.

V. QUADRUPOLE INVARIANTS AND MOMENTS OF \hat{Q}_{20}

While the axial quadrupole distribution in the laboratory frame exhibits a model-independent signature of deformation, the physical quantity of interest is the intrinsic deformation. The intrinsic quadrupole deformation parameters are usually extracted in the framework of a mean-field approximation, and the challenge is to extract them in the rotationally invariant framework of the CI shell model. Combinations of the quadrupole operators $\hat{Q}_{2\mu}$ that are invariant under rotations, known as quadrupole invariants [3, 4], have the same values in both the laboratory frame and the intrinsic frame, and thus can provide information on the effective values of the intrinsic deformation parameters without resorting to a mean-field approximation.

We define the low-order quadrupole invariants below and show that they are related to moments of \hat{Q}_{20} of the same order in the following subsection VB.

A. Quadrupole invariants

The quadrupole invariants can be classified by their order. The lowest-order invariant is quadratic

$$\hat{Q} \cdot \hat{Q} = \sum_{\mu} (-)^{\mu} \hat{Q}_{2\mu} \hat{Q}_{2-\mu}. \quad (25)$$

The third-order invariant is given by

$$(\hat{Q} \times \hat{Q}) \cdot \hat{Q} = \sqrt{5} \sum_{\mu_1, \mu_2, \mu_3} \begin{pmatrix} 2 & 2 & 2 \\ \mu_1 & \mu_2 & \mu_3 \end{pmatrix} \hat{Q}_{2\mu_1} \hat{Q}_{2\mu_2} \hat{Q}_{2\mu_3}. \quad (26)$$

There are three different ways to construct a fourth-order invariant. Under certain conditions, the fourth-

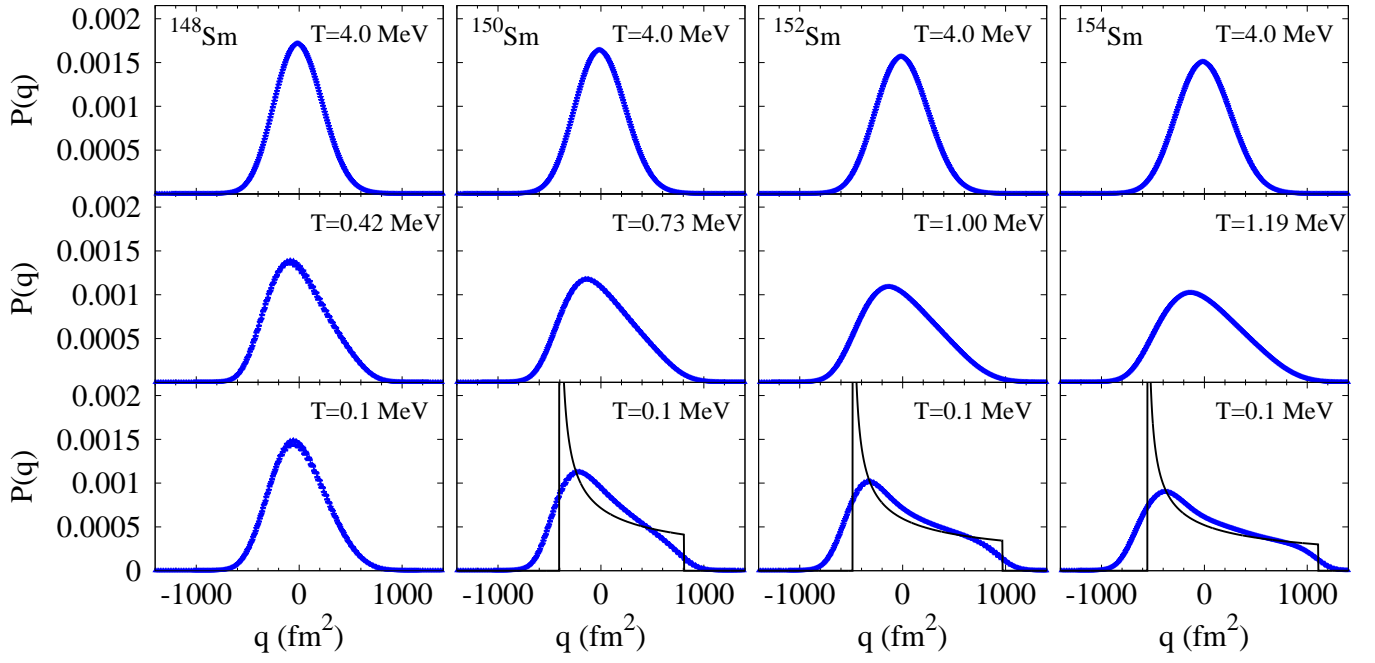


FIG. 5. Distributions $P(q)$ vs. q for an isotope chain of even-mass samarium nuclei at high temperature (top row), intermediate temperatures (middle row), and at low temperature (bottom row). In the middle row, the deformed nuclei (^{150}Sm , ^{152}Sm , ^{154}Sm) are shown near their HFB shape transition temperatures. The solid lines are the rigid-rotor distributions (23) with the ground-state HFB values of the intrinsic quadrupole moment q_0 .

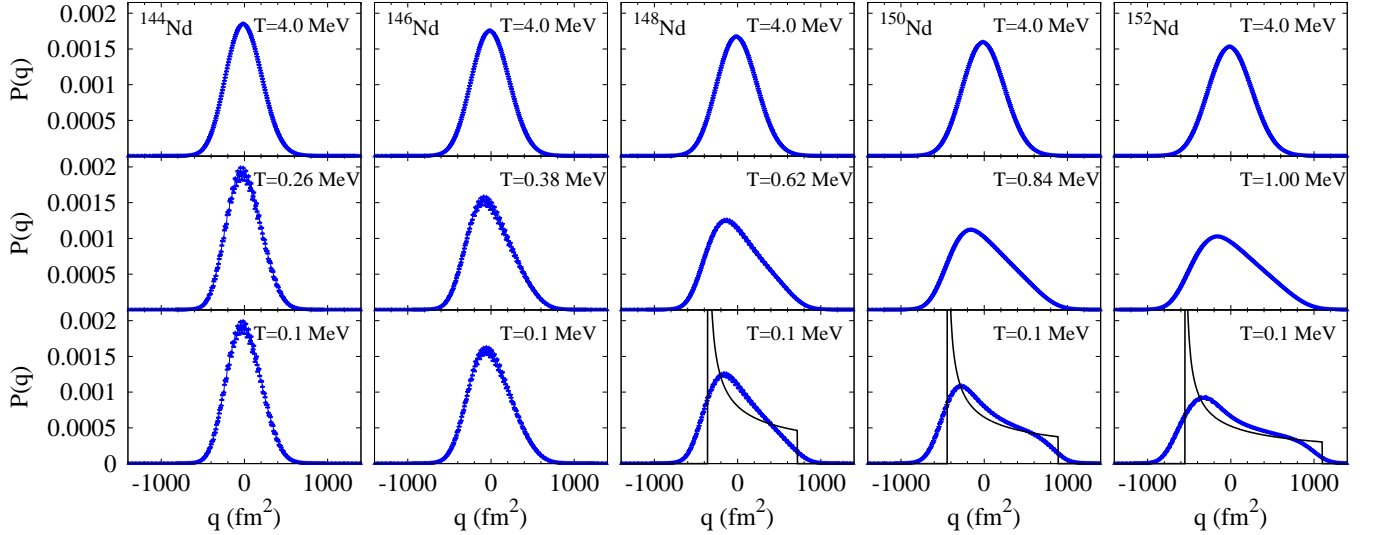


FIG. 6. As in Fig. 5 but for an isotope chain of even-mass neodymium nuclei. In the middle row, the deformed nuclei (^{148}Nd , ^{150}Nd , ^{152}Nd) are shown near their HFB shape transition temperatures.

order invariants are all proportional to $(\hat{Q} \cdot \hat{Q})^2$

$$(\hat{Q} \times \hat{Q})^{(J)} \cdot (\hat{Q} \times \hat{Q})^{(J)} = \begin{cases} \frac{1}{5}(\hat{Q} \cdot \hat{Q})^2, & J = 0 \\ \frac{2}{7}(\hat{Q} \cdot \hat{Q})^2, & J = 2 \\ \frac{18}{35}(\hat{Q} \cdot \hat{Q})^2, & J = 4 \end{cases}, \quad (27)$$

which will be derived below. Similarly, the fifth-order invariant is also unique and we define it to be $(\hat{Q} \cdot \hat{Q})((\hat{Q} \times \hat{Q}) \cdot \hat{Q})$.

To derive Eq. (27), we will assume that the quadrupole operators $\hat{Q}_{2\mu}$ commute among themselves. This holds for the quadrupole operators in coordinate space but not in the truncated CI shell model space. We believe the effect of their noncommutation is small and so we will ignore this in the following. Working in basis of simultaneous eigenstates of $\hat{Q}_{2\mu}$ with eigenvalues $q_{2\mu}$, we then rotate to an intrinsic frame, in which we will denote the

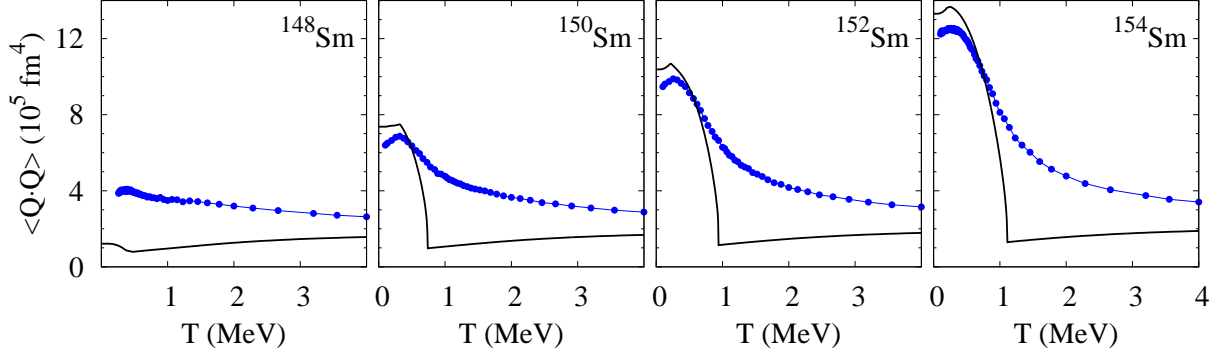


FIG. 7. $\langle \hat{Q} \cdot \hat{Q} \rangle$ for Sm isotopes. The AFMC results (solid circles) are compared with the HFB results (solid lines).

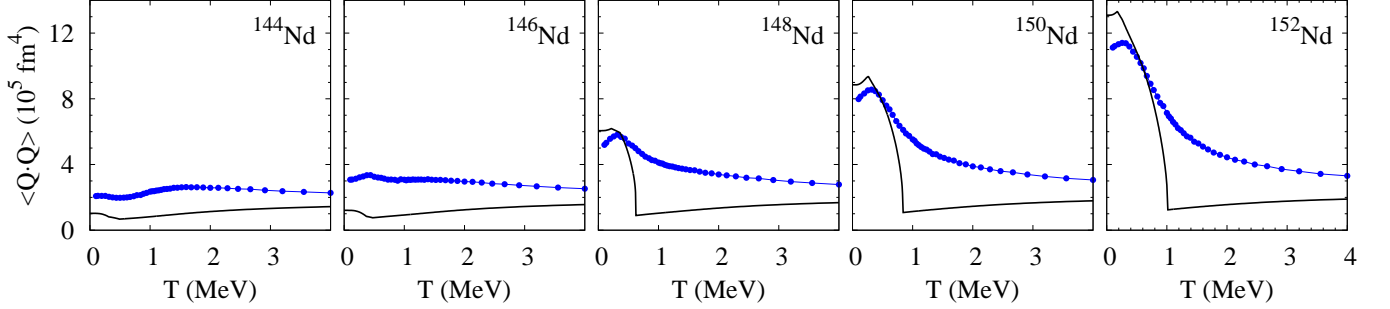


FIG. 8. $\langle \hat{Q} \cdot \hat{Q} \rangle$ for Nd isotopes. Symbols and lines are as in Fig. 7.

quadrupole components by $\tilde{q}_{2\mu}$. This frame is defined by the conditions

$$\tilde{q}_{21} = \tilde{q}_{2-1} = 0, \quad \tilde{q}_{22} = \tilde{q}_{2-2} = \text{real}. \quad (28)$$

To calculate the fourth-order invariants, we expand

$$(\tilde{q} \times \tilde{q})^{(J)} \cdot (\tilde{q} \times \tilde{q})^{(J)} = \sum_{\mu} (-)^{\mu} (\tilde{q} \times \tilde{q})_{\mu}^{(J)} (\tilde{q} \times \tilde{q})_{-\mu}^{(J)} \quad (29)$$

as well as $(\tilde{q} \times \tilde{q})_{\mu}^{(J)} = \sum (2m \ 2\mu - m | J \ \mu) \tilde{q}_{2m} \tilde{q}_{2\mu-m}$. Only terms with even μ contribute to the sum in this frame. Evaluating the Clebsch-Gordan coefficients and simplifying, one obtains

$$(\tilde{q} \times \tilde{q})^{(J)} \cdot (\tilde{q} \times \tilde{q})^{(J)} = \begin{cases} \frac{1}{5}(\tilde{q}_{20}^2 + 2\tilde{q}_{22}^2)^2, & J = 0 \\ \frac{2}{7}(\tilde{q}_{20}^2 + 2\tilde{q}_{22}^2)^2, & J = 2 \\ \frac{18}{35}(\tilde{q}_{20}^2 + 2\tilde{q}_{22}^2)^2, & J = 4. \end{cases} \quad (30)$$

Since $(\tilde{q}_{20}^2 + 2\tilde{q}_{22}^2) = \tilde{q} \cdot \tilde{q} = q \cdot q$ in this frame, we obtain Eq. (27) by rotational invariance.

B. Relations of the quadrupole invariants to moments of \hat{Q}_{20}

When the invariant is unique at a given order, its expectation value can be computed directly from the corresponding lab-frame moment of \hat{Q}_{20} , defined by $\langle \hat{Q}_{20}^n \rangle_{\beta} =$

$\int q^n P_{\beta}(q) dq$. For a rotationally invariant system, the expectations $\langle \hat{Q}_{20}^n \rangle$ for $n = 2, 3, 4$ are related to the invariants by [2]

$$\langle \hat{Q} \cdot \hat{Q} \rangle = 5 \langle \hat{Q}_{20}^2 \rangle, \quad (31)$$

$$\langle (\hat{Q} \times \hat{Q})^{(2)} \cdot \hat{Q} \rangle = -5 \sqrt{\frac{7}{2}} \langle \hat{Q}_{20}^3 \rangle, \quad (32)$$

$$\langle (\hat{Q} \cdot \hat{Q})^2 \rangle = \frac{35}{3} \langle \hat{Q}_{20}^4 \rangle, \quad (33)$$

$$\langle (\hat{Q} \cdot \hat{Q}) ((\hat{Q} \times \hat{Q}) \cdot \hat{Q}) \rangle = -\frac{11}{2} \sqrt{\frac{7}{2}} \langle \hat{Q}_{20}^5 \rangle. \quad (34)$$

We now derive Eqs. (31-33). For Eq. (31), note that $\langle \hat{Q} \cdot \hat{Q} \rangle = \sum_{\mu} (-)^{\mu} \langle \hat{Q}_{2\mu} \hat{Q}_{2-\mu} \rangle = \sum_{\mu} \langle \hat{Q}_{2\mu}^{\dagger} \hat{Q}_{2\mu} \rangle$, since $\hat{Q}_{2\mu}^{\dagger} = (-)^{\mu} \hat{Q}_{2-\mu}$ (i.e., $\hat{Q}_{2\mu}$ is an hermitian operator). But for a rotationally invariant system, $\langle \hat{T}_M^{(J)} \hat{T}_{M'}^{(J')\dagger} \rangle \propto \delta_{J,J'} \delta_{M,M'}$ and is independent of M for any spherical tensor operator $\hat{T}^{(J)}$. This leads to relation (31).

For the third moment, write

$$\langle \hat{Q}_{20}^3 \rangle = \sum_J (20 \ 20 | J0) \langle (\hat{Q} \times \hat{Q})_0^{(J)} \hat{Q}_{20} \rangle \quad (35)$$

$$= \sum_{J,K} (20 \ 20 | J0) (J0 \ 20 | K0) \langle (\hat{Q} \times \hat{Q})^{(J)} \times \hat{Q} \rangle_0^{(K)}. \quad (36)$$

Due to rotational invariance only the $K = 0$ term contributes, which also fixes $J = 2$. Using $(20 \ 20 | 20) =$

$-\sqrt{2/7}$ and $(20\ 20|00) = 1/\sqrt{5}$, we obtain Eq. (32).

The fourth moment of \hat{Q}_{20} can be calculated in a similar manner by writing

$$\langle \hat{Q}_{20}^4 \rangle = \sum_{J,J',K} (20\ 20|J0)(20\ 20|J'0)(J0\ J'0|K0) \times \langle [(\hat{Q} \times \hat{Q})^{(J)} \times (\hat{Q} \times \hat{Q})^{(J')}]_0^{(K)} \rangle. \quad (37)$$

Again only $K = 0$ contributes to the sum, requiring $J = J'$. Also $(20\ 20|J0) \neq 0$ only for $J = 0, 2, 4$. Noting that $(\hat{T}^{(J)} \times \hat{T}^{(J)})_0^{(0)} = (-)^J (\hat{T}^{(J)} \cdot \hat{T}^{(J)})/\sqrt{2J+1}$ and $(J0\ J0|00) = (-)^J/\sqrt{2J+1}$, we obtain

$$\langle \hat{Q}_{20}^4 \rangle = \sum_J \frac{(20\ 20|J0)^2}{2J+1} \langle (\hat{Q} \times \hat{Q})^{(J)} \cdot (\hat{Q} \times \hat{Q})^{(J)} \rangle. \quad (38)$$

Expressing the fourth-order invariants $\langle (\hat{Q} \times \hat{Q})^{(J)} \cdot (\hat{Q} \times \hat{Q})^{(J)} \rangle$ in terms of $(\hat{Q} \cdot \hat{Q})^2$ using Eq. (27), we find the result in Eq. (33).

Relation (34) for the fifth-order invariant can be derived in a similar manner.

C. Effective deformation parameters

We now use the quadrupole invariants to define effective deformation parameters which can be calculated from quantities known only in the lab frame. We define quadrupole deformation parameters $\alpha_{2\mu}$ using a liquid drop model for which [22]

$$q_{2\mu} = \frac{3}{\sqrt{5}\pi} 3r_0^2 A^{5/3} \alpha_{2\mu}. \quad (39)$$

The quadrupole deformation parameters in the intrinsic frame $\tilde{\alpha}_{2\mu}$ can be parametrized by the intrinsic parameters β, γ of the collective Bohr Hamiltonian (see Sec. 6B-1a of Ref. [1])

$$\tilde{\alpha}_{20} = \beta \cos \gamma; \quad \tilde{\alpha}_{22} = \tilde{\alpha}_{2-2} = \frac{1}{\sqrt{2}} \beta \sin \gamma. \quad (40)$$

We can write the quadrupole invariants in terms of $\tilde{\alpha}_{20}$ and $\tilde{\alpha}_{22}$ and then express them in terms of β, γ . The three lowest-order invariants are then given by $\beta^2, \beta^3 \cos(3\gamma)$ and β^4 .

The second- and third-order invariants can be used to define effective values of the intrinsic shape parameters β, γ

$$\beta = \frac{\sqrt{5}\pi}{3r_0^2 A^{5/3}} \langle \hat{Q} \cdot \hat{Q} \rangle^{1/2}; \quad \cos 3\gamma = -\sqrt{\frac{7}{2}} \frac{\langle (\hat{Q} \times \hat{Q}) \cdot \hat{Q} \rangle}{\langle \hat{Q} \cdot \hat{Q} \rangle^{3/2}}. \quad (41)$$

We can also define an effective fluctuation $\Delta\beta$ in β from

$$(\Delta\beta/\beta)^2 = \left[\langle (\hat{Q} \cdot \hat{Q})^2 \rangle - \langle \hat{Q} \cdot \hat{Q} \rangle^2 \right]^{1/2} / \langle \hat{Q} \cdot \hat{Q} \rangle. \quad (42)$$

Nucleus	AFMC			HFB/5DCH		
	β	$\Delta\beta/\beta$	γ (degrees)	β	$\Delta\beta/\beta$	γ (degrees)
¹⁴⁴ Nd	0.106	0.755	25.0	0.118	0.29	28.
¹⁴⁶ Nd	0.126	0.744	22.0	0.167	0.26	25.
¹⁴⁸ Nd	0.160	0.671	17.1	0.218	0.23	20.
¹⁵⁰ Nd	0.194	0.583	15.0	0.280	0.22	14.
¹⁵² Nd	0.223	0.531	14.9	0.329	0.16	10.
¹⁴⁸ Sm	0.133	0.737	22.5	0.169	0.27	25.
¹⁵⁰ Sm	0.173	0.627	16.2	0.229	0.25	20.
¹⁵² Sm	0.206	0.559	13.9	0.306	0.21	13.
¹⁵⁴ Sm	0.230	0.520	13.7	0.342	0.15	10.

TABLE I. Effective deformation parameters β, γ and relative fluctuation $\Delta\beta/\beta$ for the even-mass nuclei ^{144–152}Nd and ^{148–154}Sm computed from the AFMC. Statistical errors are approximately ± 2 in the last digit displayed. We used the 21-angle averaging AFMC results at $T = 0.1$ MeV. The last three columns on the right-hand-side show the corresponding quantities calculated in an HFB model extended to include some fluctuations about the HFB ground state [23].

Table V C shows the effective values of β and γ calculated for the two isotope chains of even-mass samarium and neodymium nuclei using Eqs. (41) and (42). Within each isotope chain, the effective values of β increase with neutron number as the nucleus becomes more deformed. The nuclei within each isotope chain also become more rigid as indicated by the decrease of $\Delta\beta/\beta$. The respective values of the effective γ decrease, being closer to triaxiality for the spherical nuclei and closer to axiality for the deformed nuclei.

The table also shows the corresponding quantities calculated in a model based on self-consistent mean field theory but including fluctuations in the deformation parameters [23]. The trends are all the same as in the AFMC results, and the triaxiality parameters agree fairly well for these two very different theories. The β parameters are systematically smaller in the AFMC. The table also shows that the fluctuation $\Delta\beta/\beta$ is significantly smaller in the HFB/5DCH than in the AFMC. This is also to be expected. The degree of freedoms that can fluctuate in the HFB/5DCH are very limited, while all the nucleonic degrees of freedom in the valence shells can participate in the AFMC fluctuations.

VI. SUMMARY AND OUTLOOK

While mean-field models of heavy nuclei are useful for a qualitative understanding of deformation, they break the rotational invariance of the underlying Hamiltonian and exhibit a nonphysical sharp shape transition as a function of temperature. We have described a method, based on Eqs. (10) and (11), to extract signatures of deformation in a framework that preserves rotational invariance. Qualitatively and at low temperatures, the mean-

field characterization of deformed nuclei is supported by the new method. However, contrary to the mean-field approximation, the new method produces smooth shape transitions as a function of temperature.

In the mean-field context, deformation is associated with an intrinsic frame. In the rotationally invariant framework, there is no well-defined intrinsic frame, since $\langle \hat{Q}_{2\mu} \rangle = 0$. However, \hat{Q}_{20} can have a nontrivial distribution in the lab frame, which we have seen can provide a model-independent signature of deformation.

The quadrupole invariants have the same values in the lab frame and in the intrinsic frame. These values can in turn be expressed in terms of moments of the axial quadrupole in the lab frame, and this enables us to obtain information about the effective intrinsic deformation parameters in the rotationally invariant framework of the CI shell model, without resorting to a mean-field approximation. We have computed from AFMC these effective quadrupole shape parameters β, γ for the isotope chains of even-mass $^{148-154}\text{Sm}$ and $^{144-152}\text{Nd}$ nuclei.

For deformed nuclei, we have seen that the AFMC expectation $\langle \hat{Q} \cdot \hat{Q} \rangle$ is quite close to the HFB value at low temperature.

Nuclear deformation plays a key role in fission processes, where the level density as a function of deformation is a crucial input to models. Since the quadrupole projection method in the lab-frame allows us to extract information about the intrinsic shape through the use of quadrupole invariants, we will show in subsequent work that it can be used to calculate the level density as a function of excitation energy and intrinsic deformation parameters β, γ .

ACKNOWLEDGMENTS

We thank J. Dobaczewski and K. Heyde for comments on the manuscript. This work was supported in part by the U.S. DOE grant Nos. DE-FG02-91ER40608 and DE-FG02-00ER41132. The research presented here used resources of the National Energy Research Scientific Computing Center, which is supported by the Office of Science of the U.S. Department of Energy under Contract No. DE-AC02-05CH11231. This work was also supported by the HPC facilities operated by, and the staff of, the Yale Center for Research Computing.

APPENDIX A: GENERAL SOLUTION FOR ROTATION ANGLES

In Sec. III B 1 we derived a set of six angles which restore rotational invariance up to the second-order moment of \hat{Q}_{20} . Here we determine the angles that restore invariance up to the n -th order moment of \hat{Q}_{20} . (Note the six-angle solution is a special case; the general solution given here yields a set of ten angles for $n = 2$.)

To begin, we express \hat{Q}_{20}^n as a sum over quadrupole invariants by successive coupling of angular momenta 2 (the rank of \hat{Q})

$$\hat{Q}_{20}^2 = \sum_J (20 \ 20 | J0) (\hat{Q} \times \hat{Q})_0^{(J)}, \quad (43a)$$

$$\hat{Q}_{20}^3 = \sum_{J_{12}, J} (20 \ 20 | J_{12} 0) (J_{12} 0 \ 20 | J0) \times [(\hat{Q} \times \hat{Q})^{(J_{12})} \times \hat{Q}]_0^{(J)}, \quad (43b)$$

⋮

$$\hat{Q}_{20}^n = \sum_{\alpha} C_{\alpha} \hat{Q}_{\alpha, M=0}^{(J)}, \quad (43c)$$

where $\alpha = (J_{12}, J_{(12)3}, \dots)$ labels the intermediate angular momenta and $\hat{Q}_{\alpha, M}^{(J)} = [(\hat{Q} \times \hat{Q})^{(J_{12})} \times \hat{Q}]^{(J_{(12)3})} \times \dots \times \hat{Q}_{1M}^{(J)}$. In Eq. (43) J takes on only even values $J = 0, 2, \dots, 2n$ because of selection rules.

Applying a rotation to \hat{Q}_{20}^n we obtain

$$\hat{R}(\Omega) \hat{Q}_{20}^n \hat{R}^{\dagger}(\Omega) = \sum_M D_{M,0}^{(J)}(\Omega) \sum_{\alpha} C_{\alpha} \hat{Q}_{\alpha, M}^{(J)}. \quad (44)$$

The general condition in order to zero out the terms for $2 \leq J \leq 2n$ by averaging over rotations $\hat{R}(\Omega_i)$ (such that only the scalar $J = 0$ term survives) is then

$$\sum_{i=1}^{N_{\Omega}} D_{M,0}^{(J)}(\Omega_i) = 0, \quad J = 2, 4, \dots, 2n, \quad -J \leq M \leq J. \quad (45)$$

Averaging over these angles will then effectively restore rotational invariance sample-by-sample for the observables $\langle \hat{Q}_{20} \rangle, \langle \hat{Q}_{20}^2 \rangle, \dots, \langle \hat{Q}_{20}^n \rangle$, and also reduce fluctuations in the distribution $P_{\beta}(q)$.

To find the angles, note that

$$\begin{aligned} D_{M0}^{(J)}(\phi, \theta, \psi) &= \sqrt{\frac{4\pi}{2J+1}} Y_J^M(\theta, \phi) \\ &= \sqrt{\frac{(J-M)!}{(J+M)!}} P_J^M(\cos \theta) e^{iM\phi}. \end{aligned} \quad (46)$$

Since $J \leq 2n$, we can project onto $M = 0$ using a Fourier sum with angles $\varphi_k = 2\pi k/(2n+1)$, $k = 0, 1, \dots, 2n$:

$$\sum_{k=0}^{2n} e^{-iM\varphi_k} = (2n+1)\delta_{M,0}, \quad -2n \leq M \leq 2n. \quad (47)$$

Then

$$\sum_{k=0}^{2n} D_M^{(J)}(\varphi_k, \theta) = (2n+1)\delta_{M,0} P_J(\cos \theta). \quad (48)$$

We now need to find angles θ_l such that $\sum_l P_J(\cos \theta_l) = 0$. Or, defining $u_l \equiv \cos \theta_l$,

$$\sum_l P_J(u_l) = 0, \quad J = 2, 4, \dots, 2n, \quad (49)$$

which is a set of n independent equations and can be satisfied by a set of n angles $\theta_l, l = 1, 2, \dots, n$.

To solve, we express the even-powered monomials u^{2m} in terms of $P_J(u)$,

$$u^{2m} = \sum_{J=0,2,\dots,2n} C_J^{(m)} P_J(u), \quad (50)$$

$$C_J^{(m)} \equiv \frac{(2J+1)(2m)!}{2^{(2m-J)/2}((2m-J)/2)!(J+2m+1)!!}, \quad (51)$$

for $m = 0, 1, \dots, n$. Then using (49)

$$\sum_{l=1}^n u_l^{2m} = C_{J=0}^{(m)} \sum_l P_0(u_l) = n/(2m+1). \quad (52)$$

So an equivalent set of equations to solve is

$$\frac{1}{n} \sum_{l=1}^n u_l^{2m} = \frac{1}{2m+1}, \quad m = 1, 2, \dots, n. \quad (53)$$

The set of $n(2n+1)$ angles (θ_l, φ_k) then satisfy

$$\frac{1}{n(2n+1)} \sum_{l=1}^n \sum_{k=0}^{2n} D_{M0}^{(J)}(\theta_l, \phi_k) = \delta_{M,0} \delta_{J,0} \quad (54)$$

for $J = 0, 2, \dots, 2n$ and $-2n \leq M \leq 2n$.

1. 10-angle solution for $n = 2$

Setting $n = 2$ in the general solution gives a set of 10 angles, different from the 6 angles discussed in Sec. III B 1. The azimuthal angles are

$$\varphi_k = 2\pi k/5, \quad k = 0, 1, \dots, 4, \quad (55)$$

and the angles θ_l are determined by the equations

$$u_1^2 + u_2^2 = 2/3 \quad (56)$$

$$u_1^4 + u_2^4 = 2/5. \quad (57)$$

with solution

$$\cos^2 \theta_1 = (1 + 2/\sqrt{5})/3 \quad (58)$$

$$\cos^2 \theta_2 = (1 - 2/\sqrt{5})/3. \quad (59)$$

2. 21-angle solution for $n = 3$

For $n = 3$, the azimuthal angles are

$$\varphi_k = 2\pi k/7, \quad k = 0, 1, \dots, 6, \quad (60)$$

and the θ_l are determined by the equations

$$u_1^2 + u_2^2 + u_3^2 = 1 \quad (61)$$

$$u_1^4 + u_2^4 + u_3^4 = 3/5 \quad (62)$$

$$u_1^6 + u_2^6 + u_3^6 = 3/7, \quad (63)$$

with solution

$$\cos^2 \theta_1 = 0.7504 \dots \quad (64)$$

$$\cos^2 \theta_2 = 0.1785 \dots \quad (65)$$

$$\cos^2 \theta_3 = 0.0711 \dots \quad (66)$$

This gives a set of 21 angles that is sufficient to thermalize the distribution of \hat{Q}_{20} , as shown in Fig. 2.

APPENDIX B: LAB-FRAME QUADRUPOLE MOMENTS FOR THE RIGID ROTOR

The moments of the rigid-rotor distribution (23) can be calculated in terms of q_0 from a simple recursion relation. To calculate the moments $\langle q^n \rangle$, we derive a recursion formula as follows. Measuring q in units of q_0 , i.e., $x = q/q_0$, we use integration by parts to find

$$\begin{aligned} \int dx \frac{x^n}{\sqrt{1+2x}} &= x^n \sqrt{1+2x} - n \int dx x^{n-1} \sqrt{2x+1} \\ &= x^n \sqrt{1+2x} - n \int dx x^{n-1} \frac{2x+1}{\sqrt{2x+1}} \end{aligned}$$

or

$$(2n+1) \int dx \frac{x^n}{\sqrt{1+2x}} = x^n \sqrt{1+2x} - n \int dx \frac{x^{n-1}}{\sqrt{2x+1}}. \quad (67)$$

Taking the limits between $-1/2$ and 1, the n -th moment $\langle x^n \rangle = \frac{1}{\sqrt{3}} \int_{-1/2}^1 dx \frac{x^n}{\sqrt{1+2x}}$ satisfies the recursion relation

$$\langle x^n \rangle = \frac{1}{2n+1} (1 - n \langle x^{n-1} \rangle). \quad (68)$$

Starting with $\langle q^0 \rangle = 1$ (normalization), we can use Eq. (68) to calculate the first few moments

$$\langle q \rangle = 0; \quad \langle q^2 \rangle = \frac{1}{5} q_0^2; \quad \langle q^3 \rangle = \frac{2}{35} q_0^3; \quad \langle q^4 \rangle = \frac{3}{35} q_0^4; \dots \quad (69)$$

[1] A. Bohr and B. Mottelson, *Nuclear Structure*, Vol. II (Benjamin, 1975).

[2] Y. Alhassid, C.N. Gilbreth, and G.F. Bertsch, Phys. Rev. Lett. **113**, 262503 (2014).

- [3] K. Kumar, Phys. Rev. Lett. **28**, 249 (1972).
- [4] D. Cline, Ann. Rev. Nucl. Part. Sci. **36**, 683 (1986).
- [5] K. Hadyńska-Klek, P. J. Napiorkowski, M. Zielińska, J. Srebrny, A. Maj, F. Azaiez, J. J. Valiente Dobón, M. Kicińska-Habior, F. Nowacki, H. Naïdja et al., Phys. Rev. Lett. **117**, 062501 (2016).
- [6] T. Schmidt, K. L. G. Heyde, A. Blazhev, and J. Jolie, Phys. Rev. C **96**, 014302 (2017).
- [7] Y. Alhassid, G.F. Bertsch, D.J. Dean, and S.E. Koonin, Phys. Rev. Lett. **77**, 1444 (1996).
- [8] A.L. Goodman, Nucl. Phys. **A352**, 30 (1981).
- [9] K. Tanabe, K. Sugawara-Tanabe and H.J. Mang, Nucl. Phys. **A357** 20 (1981).
- [10] G.H. Lang, C.W. Johnson, S.E. Koonin, and W.E. Ormand, Phys. Rev. C **48**, 1518 (1993).
- [11] Y. Alhassid, D.J. Dean, S.E. Koonin, G. Lang, and W.E. Ormand, Phys. Rev. Lett. **72**, 613 (1994).
- [12] For a recent review, see Y. Alhassid in *Emergent Phenomena in Atomic Nuclei from Large-Scale Modeling: a Symmetry-Guided Perspective*, edited by K. D. Launey (World Scientific, Singapore, 2017).
- [13] J. Hubbard, Phys. Rev. Lett. **3**, 77 (1959); R. L. Stratonovich, Dokl. Akad. Nauk SSSR [Sov. Phys. - Dokl.] **115**, 1097 (1957).
- [14] W.E. Ormand, D.J. Dean, C.W. Johnson, G.H. Lang, and S.E. Koonin, Phys. Rev. C **49**, 1422 (1994).
- [15] Y. Alhassid, S. Liu, and H. Nakada, Phys. Rev. Lett. **83**, 4265 (1999).
- [16] Y. Alhassid, S. Liu, and H. Nakada, Phys. Rev. Lett. **99**, 162504 (2007).
- [17] Y. Alhassid, L. Fang and H. Nakada, Phys. Rev. Lett. **101**, 082501 (2008).
- [18] C. Özen, Y. Alhassid, and H. Nakada, Phys. Rev. Lett. **110**, 042502 (2013).
- [19] A.L. Goodman, Phys. Rev. C **33**, 2212 (1986).
- [20] V. Martin, J. L. Egido and L. M. Robledo, Phys. Rev. C **68**, 034327 (2003).
- [21] B. K. Agrawal, T. Sil, J. N. De, and S. K. Samaddar, Phys. Rev. C **62**, 044307 (2000).
- [22] See for example in P. Ring and P. Schuck, *The Nuclear Many-Body Problem* (Springer-Verlag, New York, 1980).
- [23] J.-P. Delaroche, M. Girod, J. Libert, H. Goutte, S. Hilaire, S. Péru, N. Pillet, and G. F. Bertsch, Phys. Rev. C **81**, 014303 (2010).